Climate Dynamics (2006) 27: 261–279
DOI 10.1007/s00382-006-0138-4

Matthew C. Wyant · Christopher S. Bretherton
Julio T. Bacmeister · Jeffrey T. Kiehl
Isaac M. Held · Ming Zhao · Stephen A. Klein
Brian J. Soden

A comparison of low-latitude cloud properties and their response to climate change in three AGCMs sorted into regimes using mid-tropospheric vertical velocity

Received: 16 August 2005 / Accepted: 28 February 2006 / Published online: 5 May 2006

Abstract Low-latitude cloud distributions and cloud responses to climate perturbations are compared in near-current versions of three leading U.S. AGCMs, the NCAR CAM 3.0, the GFDL AM2.12b, and the NASA GMAO NSIPP-2 model. The analysis technique of Bony et al. (Clim Dyn 22:71–86, 2004) is used to sort cloud variables by dynamical regime using the monthly mean pressure velocity ω at 500 hPa from 30S to 30N. All models simulate the climatological monthly mean top-of-atmosphere longwave and shortwave cloud radiative forcing (CRF) adequately in all ω-regimes. However, they disagree with each other and with ISCCP satellite observations in regime-sorted cloud fraction, condensate amount, and cloud-top height. All models have too little cloud with tops in the middle troposphere and too much thin cirrus in ascent regimes. In subsidence regimes one model simulates cloud condensate to be too near the surface, while another generates condensate over an excessively deep layer of the lower troposphere. Standardized climate perturbation experiments of the three models are also compared, including uniform SST increase, patterned SST increase, and doubled CO_2 over a mixed layer ocean. The regime-sorted cloud and CRF perturbations are very different between models, and show lesser, but still significant, differences between the same model simulating different types of imposed climate perturbation. There is a negative correlation across all general circulation models (GCMs) and climate perturbations between changes in tropical low cloud cover and changes in net CRF, suggesting a dominant role for boundary layer cloud in these changes. For some of the cases presented, upper-level clouds in deep convection regimes are also important, and changes in such regimes can either reinforce or partially cancel the net CRF response from the boundary layer cloud in subsidence regimes. This study highlights the continuing uncertainty in both low and high cloud feedbacks simulated by GCMs.

M. C. Wyant (✉) · C. S. Bretherton
Department of Atmospheric Sciences,
University of Washington, Box 351640, Seattle
WA 98195, USA
E-mail: mwyant@atmos.washington.edu
Tel.: +1-206-6859526
Fax: +1-206-6859302

J. T. Bacmeister
NASA Global Modeling and Assimilation Office,
Goddard Spaceflight Center, Greenbelt, MD, USA

J. T. Kiehl
National Center for Atmospheric Research,
Boulder, CO, USA

I. M. Held · M. Zhao · S. A. Klein · B. J. Soden
NOAA Geophysical Fluid Dynamics Laboratory,
Princeton, NJ, USA

S. A. Klein
The Atmospheric Science Division,
Lawrence Livermore National Laboratory,
Livermore, CA, USA

B. J. Soden
Division of Meteorology and Physical Oceanography,
Rosenstiel School of Marine and Atmospheric Science,
University of Miami, Miami, FL, USA

1 Introduction

The representation of clouds in climate models continues to be a difficult and significant challenge to the climate research community. Cloud radiative feedbacks account for a significant portion of the variation in the response of climate models to increases in global CO_2 concentrations (e.g., Senior and Mitchell 1996; Cess et al. 1996).

Zhang et al. (2005) compared the simulated climates of a large group of atmospheric general circulation models (GCMs) with observations from the interna-

tional satellite cloud climatology project (ISCCP; Rossow and Schiffer 1999) and from the clouds and the earth's radiant energy system (CERES; Smith et al. 2004) project. They compared the measured and modeled cloud fraction at various cloud-top heights and optical thicknesses and found significant model-dependent discrepancies for many categories of clouds. The differences in top-of-atmosphere (TOA) longwave and shortwave cloud radiative forcing (CRF) between the models and observations were not as large, due to compensating errors in predicting cloud fraction at various heights and thicknesses. Given these differences in representing clouds in the current climate in GCMs, it is not surprising that the models' responses to a climate perturbation vary significantly.

Low-latitude clouds are tightly connected to the seasonally varying mean overturning circulation. In the ascending branch there are extensive deep-convective cloud systems; the subsiding branch is dominated by boundary layer cumulus and stratocumulus. This tight connection can partly be seen in zonal-average plots or regional analyses (e.g., Lin and Zhang 2004). It is even better encapsulated in an analysis methodology popularized by Bony et al. (2004), hereafter referred to as B04, which sorts the tropics into dynamical regimes based on the monthly mean pressure velocity at 500 hPa (ω_{500}). Bony used this to compare the tropical climatology of shortwave cloud forcing (SWCF) and longwave cloud forcing (LWCF) in three European GCMs and their cloud radiative response to a climate perturbation.

Williams et al. (2003) sort with respect to both ω_{500} and SST in order to analyze tropical cloudiness in multiple versions of the Hadley Center model, HadAM, and to compare with earth radiation budget experiment (ERBE) radiation and ISCCP cloud climatologies. Sorting with respect to SST adds complexity but allows clearer separation of stratocumulus and shallow cumulus regimes, which are both present in subsidence regimes with comparable climatological ω_{500}. They also interpreted modeled responses to climate perturbations by sorting by the local change in SST and ω_{500}.

Here we use Bony's methodology to compare the representation of tropical clouds in three current U.S. GCMs. In Sect. 2 we describe the models, the observational, and reanalysis data, and the simulations performed. In Sect. 3 we briefly review the sorting method of B04 used throughout this study. Section 4 examines the cloud-related properties in the GCM model climatologies and compares them with observations. The GCM-predicted cloud fraction statistics based on 'ISCCP simulator' software are compared with ISSCP data for two of the GCMs in Sect. 5. The responses of the modeled tropical clouds to a +2K increase in SST are presented in Sect. 6. Model responses to a broader range of climate perturbations are examined in Sect. 7. In Sect. 8 we discuss and summarize the results. Because the three models exhibit quite different responses (also found by B04) we did not add to the complexity of this study by also sorting by SST, though this might prove valuable in the future.

2 Data, model, and experiment descriptions

2.1 Description of observational and reanalysis data

The ISCCP D1 cloud data set, obtained from the Langley Distributed Active Archive Center, consists of revised-algorithm ISCCP DX satellite-pixel-level data that has been spatially averaged onto a global equal-area 280 km grid. The raw cloud fraction data are provided every 3 h for daylight hours only. The data used in this study span the period from July 1983 to September 2001. Monthly means of the cloud fraction were computed on the native ISCCP grid and interpolated to a regular 2.8°×2.8° grid. The D1 cloud fraction is binned into six optical thickness categories, each of which is further subdivided into seven cloud-top pressure categories.

From ERBE shortwave and longwave cloud forcing data (Harrison et al. 1990) monthly climatologies were constructed for the period 1986–1989 on a 2.8° latitude×2.8° longitude grid. Special sensor microwave imager (SSMI) liquid water path and water vapor path monthly climatologies were created for the period 1987–2000. A TRMM microwave imager (TMI) liquid water path climatology was also constructed from a 2 year set of observations from 1999 to 2000 (Wood et al. 2002). Both SSMI and TMI climatologies use the algorithm of Wentz (1997) and were interpolated onto the same 2.8° latitude×2.8° longitude grid.

National Centers for Environmental Prediction (NCEP) reanalysis data (Kalnay et al. 1996) from 1979 to 1998 and European Centre for Medium-Range Weather Forecasts (ECMWF) ERA-40 reanalysis data (Uppala et al. 2005) from 1980 to 2001 were each used to create monthly ω_{500} climatologies on a 2.8° latitude×2.8° longitude grid. These are used together with the ERBE data for comparisons with the GCM outputs.

2.2 Description of AGCM simulations

The three AGCMs used in this study are the National Center for Atmospheric Research (NCAR) Community Atmospheric Model (CAM) 3.0 (Collins et al. 2004), the Geophysical Fluid Dynamics Laboratory (GFDL) Atmospheric Model (AM) 2.12b (GFDL Global Atmospheric Model Development Team 2004), and the NASA Global Modeling and Assimilation Office (GMAO) NSIPP-2 model. The CAM runs use a preliminary version (CAM2.02_rio33) of CAM 3.0. The NSIPP-2 is a development AGCM which shares many properties of the GMAO GEOS-5 released in April 2005. The physical parameterizations of the three GCMs in this study are summarized in Table 1. While both the GMAO and GFDL models use a relaxed Arakawa–Schubert (RAS) schemes (Moorthi and Suarez 1992) for

Table 1 AGCM physics and boundary conditions

Physical component	CAM 3.0 (Collins et al. 2004)	GFDL AM2.12B (GFDL AMDT 2004)	GMAO NSIPP-2
Deep convection	Zhang and McFarlane (1995)	Relaxed Arakawa–Schubert (Moorthi and Suarez 1992)	Relaxed Arakawa–Schubert (Moorthi and Suarez 1992)
Shallow convection	Hack (1994)	Relaxed Arakawa–Schubert (Moorthi and Suarez 1992)	Relaxed Arakawa–Schubert (Moorthi and Suarez 1992)
Boundary layer	Non-local diffusion (Holtslag and Boville 1993; Vogelezang and Holtslag 1996)	Lock et al. (2000) modified for stratocumulus-top entrainment	First order (Louis et al. 1982)
Condensation	Temperature-based liquid/ice partitioning (Rasch and Kristjansson 1998; Zhang et al. 2003)	Prognostic cloud liquid, cloud ice, and cloud fraction, diagnostic rain/snow	Prognostic condensate from RAS. Temperature-based liquid/ice partitioning
Cloud microphysics	Chen and Cotton (1987) and Lin et al. (1983)	Rotstayn (1997), mixed-phase (Rotstayn et al. 2000)	Del Genio et al (1996) and Sud and Walker (1999)
Fractional cloudiness	Maximum of the following three cloud fractions: (1) stratus: Klein and Hartmann (1993); (2) layered: RH threshold; (3) convective: detrained mass flux	Modified scheme (Tiedtke 1993)	Stratiform: RH based, convective: based on detrained mass flux
Overlap	Maximum-random (Collins et al. 2004)	Random	Maximum-random
SST climatology	HadISST (Rayner et al. 2003) and Reynolds and Smith (1994)	Reynolds and Smith (1994)	Reynolds and Smith (1994)

shallow and deep convection, the implementations are different and behave differently. Another feature of the GFDL RAS scheme is the Tokioka et al. (1988) entrainment rate limiter that prevents undiluted cumulus updrafts. The AGCM grid resolutions are given in Table 2.

A series of AGCM simulations, summarized in Table 3, are analyzed in this study. Two main categories of SST boundary conditions are considered: either prescribed-SST, or a 50 m slab-ocean model coupled to the atmospheric GCM. For the prescribed-SST runs, the control case for each model uses a monthly SST climatology (see Table 1).

Three SST perturbations from the control run are considered; spatially uniform perturbations of +2K and −2K (as in Cess et al. 1996) and a spatially and monthly varying SST perturbation (ΔCMIP) based on the phase 2 of the coupled model intercomparison project (CMIP; Meehl et al. 2000). In this intercomparison, global CO_2 concentrations were slowly increased at 1% per year such that at year 70 the CO_2 concentrations were approximately double the initial concentrations. For each model, a monthly SST perturbation climatology was computed by taking the monthly mean SST from years 61–80 and subtracting from it a fixed-CO_2 control case's monthly mean SSTs over the same time interval. The SST perturbation that we use is the ensemble average of the perturbation climatology of nine CMIP GCMs.

Two simulations with a slab-ocean model are performed with the CAM and GFDL models, a control case with modern concentrations of CO_2 (355 ppm for CAM and 356 ppm form GFDL) and a perturbation case with doubled CO_2 concentrations. For both the specified SST and the slab-ocean model runs, a monthly climatology is constructed from 10 to 25 years of simulation after a model spin-up period sufficient to reach equilibrium.

For comparison of the CAM and GFDL models with ISCCP data, we utilize Atmospheric Model Intercomparison Project (AMIP) simulations with observed SSTs smoothed on a monthly time scale. Both models include an ISCCP simulator (Klein and Jakob 1999; Webb et al. 2001) to produce cloud fraction statistics (The ISSCP simulator is not implemented in the NASA GMAO model). The ISCCP simulator represents each model column as an ensemble of subcolumns. Synthetic ISCCP measurements of cloud-top

Table 2 AGCM resolution

Model	Vertical levels	Horizontal resolution		Spectral resolution
		Latitude	Longitude	
CAM AMIP run	26	1.4°	1.4°	T85
CAM other runs	26	2.8°	2.8°	T42
GFDL	24	2°	2.5°	–
GMAO	40	2°	2.5°	–

Table 3 Simulation parameters

Run name	SST	Model	SST climatology period	Averaging period (years)
Forecast analyses	Climatology	ECMWF ERA-40	1980–2001	22
		NCEP	1979–1998	20
Control	Climatology	CAM	1979–1999	10
		GFDL	1983–1991	10
		GMAO	1980–1989	10
+2K	Control +2K	CAM	–	10
		GFDL	–	10
		GMAO	–	10
−2K	Control −2K	GFDL	–	10
		GMAO	–	10
ΔCMIP	Control + CMIP perturbation	CAM	–	5
		GFDL	–	10
Slab-ocean control	Internal	CAM	–	10
		GFDL	–	25
Slab-ocean $2\times CO_2$	Internal	CAM	–	10
		GFDL	–	25
AMIP	AMIP (monthly observed)	CAM	–	1984–2000
		GFDL	–	1983–1998

pressure and cloud optical thickness are calculated based on the cloud distribution in the sub-columns, the models' particular cloud-overlap assumptions, and the ISCCP retrieval algorithm. ISCCP cloud-top can be strongly biased when multiple cloud layers are present (Klein and Jakob 1999). Monthly climatologies of ISCCP statistics are computed after a spin-up period of approximately 6 years and 1 year for the CAM and GFDL runs, respectively.

3 ω decomposition

We follow the methodology and notation of B04 for partitioning any desired field C defined over atmospheric columns within some given horizontal domain and set of times. Consider the population of columns whose ω_{500} lies within some given range of values. The area weighted mean C within in this population is

$$C_\omega = \frac{\sum_i \sigma_i C_i}{\sum_i \sigma_i}, \tag{1}$$

where σ_i is the horizontal area of a particular column, C_i is the value of the quantity, and the summation is over this particular population. If we then discretely partition an entire population of columns (that spans some horizontal spatial domain and set of times) based on ω_{500}, we can compute a discrete normalized probability density function (PDF) of the population, P_ω. For a particular population of columns corresponding to some range of ω_{500},

$$P_\omega = \frac{\sum_i \sigma_i}{\sum \sigma}, \tag{2}$$

where the denominator is the sum over all columns and times, and

$$\Sigma_\omega P_\omega = 1, \tag{3}$$

where the summation is over all ω_{500} 'bins.' If we consider a basic state and some perturbed state, the mean change in C averaged over the horizontal domain, $\overline{\delta C}$, can be computed in terms of the partitioned quantity as

$$\overline{\delta C} = \Sigma_\omega C_\omega \delta P_\omega + \Sigma_\omega P_\omega \delta C_\omega + \Sigma_\omega \delta C_\omega \delta P_\omega. \tag{4}$$

In B04, these terms are referred to as the dynamic term ($C\delta P$), the thermodynamic term ($P\delta C$), and the covarying term ($\delta P \delta C$). (Since monthly mean ω_{500} does not capture the complete range of dynamical processes, the rectified effects of higher-frequency dynamics and other dynamical processes may be subsumed in the 'thermodynamic' term.) Note that this partitioning can be applied to any desired geographical region. For example it could be applied only to areas with an ocean surface. It can be applied to a three-dimensional field by separately analyzing the field at each discrete pressure level. When a particular pressure surface intersects land, the area of intersection is excluded from the analysis.

We apply this method from 30S to 30N. This domain is particularly attractive because the ω_{500} annually averaged over this region is very small, i.e., there is a balance between columns with ascending and subsiding motions. Of course, this does not imply that the tropics are a closed system; lateral atmospheric heat divergence out of this region associated with transient baroclinic eddies and quasi-steady zonally asymmetric circulations exceeds 30 W m^{-2} in area-average (e.g., Trenberth and Caron 2001).

Following B04, we partition the ω_{500} field in 10-hPa day^{-1}-wide bins extending from −100 to 100 hPa day^{-1}, centered at −5, +5, −15, +15 hPa day^{-1}, etc. Two additional bins are used for values < -100 hPa day^{-1} and > 100 hPa day^{-1}. The maximum fraction of column-months contained in these

extreme bins for any of the models is 1.4 and 0.3%, respectively. We use monthly climatologies from multi-year GCM simulations (10 years in most cases), compared to 18 months of GCM output analyzed by B04. This reduces dynamical noise that adds uncertainty to their results.

4 Analysis of the control cases

We first compare control runs of the models where the SST is specified from external climatology. As in B04, sorting the model monthly climatologies using ω_{500} highlights significant differences between models.

Figure 1 shows climatological maps of annual-mean ω_{500} for the region 30N–30S for the ECMWF and NCEP reanalyses and the prescribed-SST control cases of the three GCMs. The GCMs and reanalyses show substantial qualitative agreement, though the strengths and locations of the ascent regions do vary noticeably between models. The GMAO model climatology shows substantial unphysical oscillations near large topography.

The PDFs of monthly mean ω_{500} for the reanalyses and the GCMs are plotted in Fig. 2. The distributions are very similar, with all the distributions peaking at 15 or 25 hPa day^{-1}. The PDFs of the GCMs agree with another fairly well and fall within or close to the range spanned by the two reanalyses, though with slightly more peaked distributions. Especially in the tropics, reanalyzed ω_{500} fields may include errors due to the sparsity of observations and physical parameterization errors in the reanalysis models. However, the good agreement between the models and reanalyses is reassuring, and it suggests that Bony-binning may average out much of the potential reanalysis error.

Of particular climatological interest is the TOA cloud forcing, introduced in Charlock and Ramanathan (1985). We define the LWCF as the difference between the clear-sky net upward longwave flux, LW_{clear}, and the net upward longwave flux, LW, at the top of the atmosphere:

$$LWCF = LW_{clear} - LW, \tag{5}$$

and similarly:

$$SWCF = SW - SW_{clear} \tag{6}$$

where SW and SW_{clear} are net downward shortwave fluxes at the top of the atmosphere. Note that changes in cloud forcing are related to but not the same as cloud feedbacks (e.g., Soden et al. 2004). Figure 3 shows ERBE cloud forcing data binned with ω_{500} from ECMWF or NCEP analyses compared to the GCM cloud forcing sorted by GCM ω_{500}. The points in Fig. 3 show ERBE data versus ECMWF ω_{500} for a random 3% subsample of individual column-months. The black and red 'X' symbols show the mean of the ERBE data within 10 hPa day^{-1} bins based on NCEP and ECMWF ω_{500} fields, respectively. The corresponding bars indicate the 25th to 75th percentile ranges of the NCEP and ECMWF bin populations. Solid lines indicate the bin-mean cloud forcings from the GCMs. The observed scatter and bars give a sense of how much of the observed

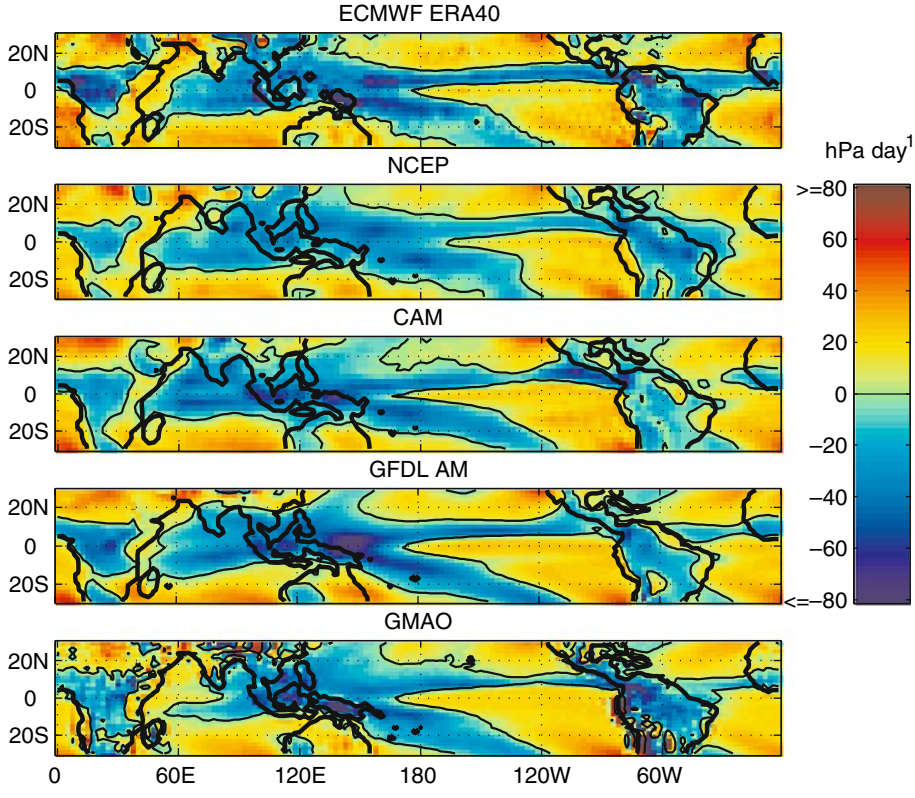

Fig. 1 Mean annual pressure velocity at the 500 hPa level, ω_{500}, in hPa day^{-1} for ECMWF and NCEP reanalysis climatologies, and for CAM, GFDL AM, and GMAO climatologies for the prescribed-SST control case. The *thin solid line* indicates $\omega_{500} = 0$

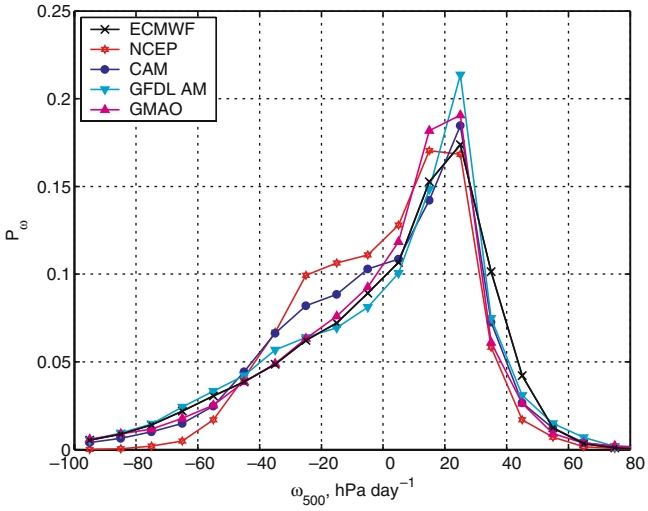

Fig. 2 PDF of monthly mean omega at 500 mb for ECMWF ERA-40 and NCEP reanalyses, and for the CAM, GFDL, and GMAO control runs

space–time variation in CRF is captured by ω_{500} binning. In the ascent regimes ($\omega_{500} < 0$) most of the variance in both LWCF and SWCF is captured. The ω_{500} binning is less successful in the subsidence regimes ($\omega_{500} > 0$), particularly in capturing SWCF variations between columns. Overall the spatial variation of cloud forcing dominates the overall variation. The seasonal range of mean LWCF and SWCF for each bin is generally less than 10 W m^{-2}, except for SWCF in strong subsidence regimes ($\omega_{500} > 20$ hPa day^{-1}) where it exceeds 20 W m^{-2}.

For $\omega_{500} < 20$ hPa day^{-1}, the LWCF has a strong downward linear trend with ω_{500}, both for ERBE data and the model output. This indicates more high clouds with decreasing ω_{500} (more mean ascent). In subsidence regimes with $\omega_{500} > 20$ hPa day^{-1}, where boundary layer clouds with low, warm tops dominate, the LWCF flattens to about 15 W m^{-2}. The models agree fairly well with the ERBE/analysis data and with each other, with the largest disparities when ω_{500} is at its most extreme. Since LWCF and SWCF are fields widely used for evaluating GCM cloud simulations, this agreement perhaps reflects model calibration to the ERBE dataset as much as physical veracity of the simulated clouds, as we will see later.

The SWCF mirrors the LWCF, but there is significantly more scatter in the ERBE data not explained by ω_{500}. The SWCF is most negative in the ascent regimes where ω_{500} is most negative (and deep convection is strongest). For $\omega_{500} > 15$ hPa day^{-1}, the relation between ω_{500} and SWCF changes slope drastically, and the scatter in the SWCF becomes pronounced due to ω_{500} bins that include both trade cumulus and stratocumulus of much more negative SWCF. As with the LWCF, the GCMs agree reasonably well with ERBE and with each other. These relationships between cloud forcing and ω_{500} also hold for daily mean model output data, but show 50–100% more scatter in cloud forcing, suggesting that daily ω_{500} is not as useful a tool for sorting cloud regimes.

The net cloud forcing (Fig. 3c) shows the high degree of cancellation of LWCF and SWCF outside the subsidence regimes (Kiehl and Ramanathan 1990). The GCMs again agree quite well with ERBE, except for

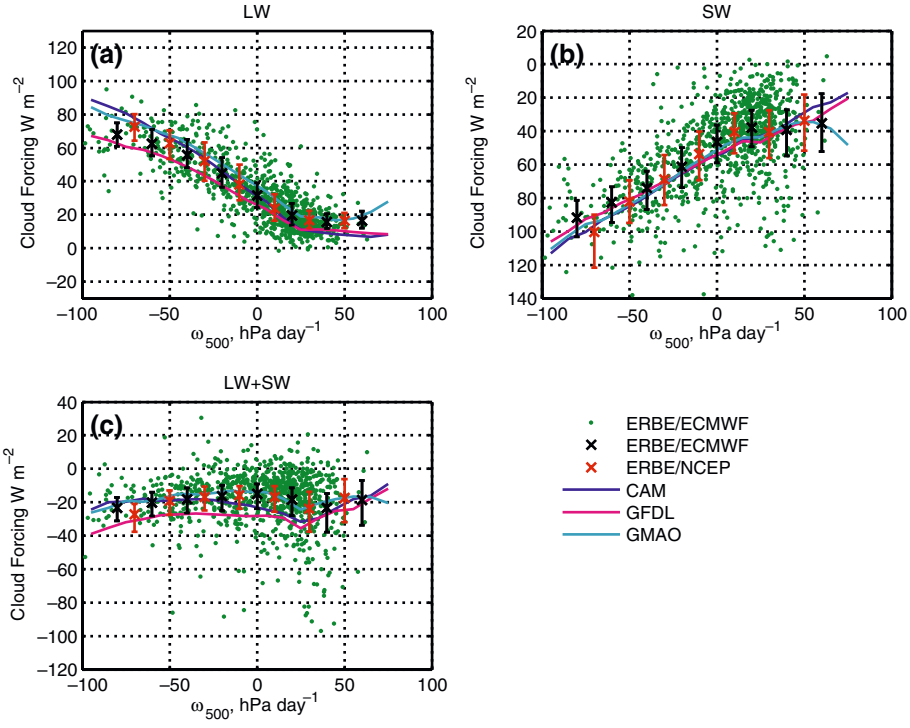

Fig. 3 **a** Longwave, **b** shortwave, and **c** net cloud forcing in W m^{-2} as a function of pressure velocity. ERBE observations sorted by ECMWF ω_{500} are plotted as *green points* (only 3% of the points are plotted). The mean ('X'), and 25th and 75th percentiles (*bars*) for ECMWF and NCEP sorted ERBE observations are plotted in *black* and *red*, respectively. The GCM ω_{500}-binned cloud forcing for the control runs are plotted as *solid lines*

excessively negative net cloud forcing in the weak-subsidence bins, ($\omega_{500} \approx 20$ hPa day^{-1}), mainly due to excessively negative SWCF in those regimes (a 'bright cloud' bias in the subtropical trade cumulus regime).

Figures 4 and 5 show the ω_{500}-binned profiles of horizontal temperature perturbation from the 30S to 30N monthly mean, relative humidity, cloud fraction, and cloud condensate for the CAM, GFDL, and GMAO control runs (points where pressure surfaces intersect land are discarded from the means). Figure 4 also includes horizontal temperature perturbation and relative humidity for the NCEP and ECMWF reanalysis climatologies. In Figs. 4 and 5 and many subsequent figures, the x-axis is stretched linearly in proportion to the PDF of ω_{500}, so that the tropics-wide average of a quantity is its horizontal average across the area on the plot.

In Fig. 4a vertically distributed warm temperature perturbations are seen in all models in the ascent regime, particularly for $\omega_{500} < -20$ hPa day^{-1}, with vertically distributed cool perturbations in regimes of strong subsidence. The reverse signature is seen at 100 hPa due to an elevated, cooler tropopause over the ascent regimes. These features reflect the thermally direct Hadley–Walker circulation. In all three GCMs and in the reanalyses, the warm perturbations in the strong ascent regimes are less pronounced in the mid-troposphere than in the lower and upper troposphere; this is particularly sharply defined in the CAM.

Figure 4b shows the relative humidity with respect to liquid water for the AGCMs and the reanalyses, indicating noticeable inter-model differences in relative humidity. All models have high relative humidities near the surface across dynamical regimes associated with the marine boundary layer, with only slight differences between models. Above the boundary layer, striking inter-model differences are found in the ascent regimes. In these bins, the CAM model shows a comparatively low relative humidity with vertical undulations in the mid-troposphere. The local relative humidity maximum at around 600 hPa is associated with the minimal warm

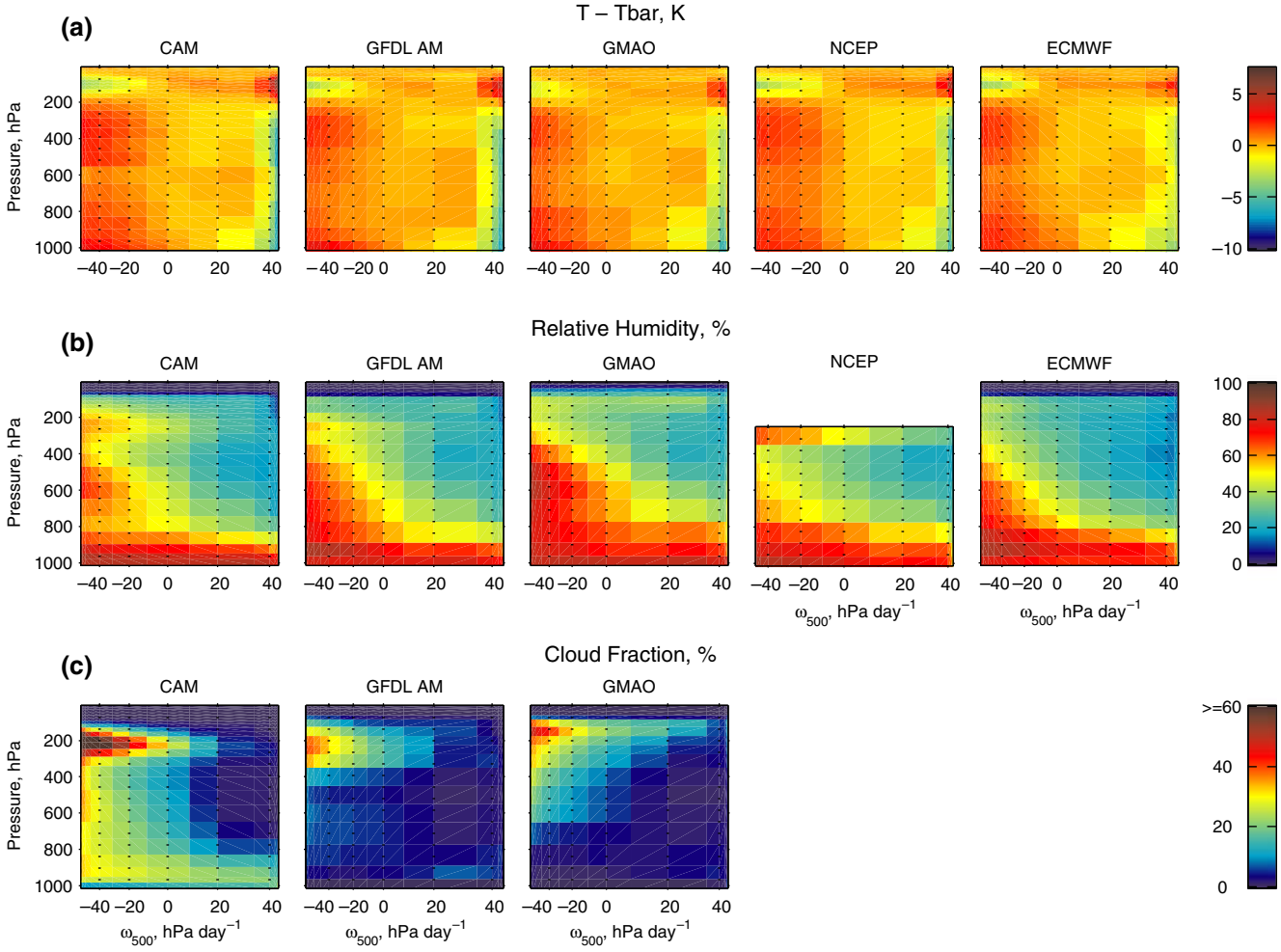

Fig. 4 **a** Mean monthly temperature perturbation (from the mean at a given pressure level) in K, **b** relative humidity (with respect to liquid water saturation) in percent, and **c** cloud fraction for the three GCM control simulations and the NCEP and ECMWF reanalyses, sorted by ω_{500} at each pressure level. The x-axis is stretched in proportion to the PDF of ω_{500}. There are two bins represented between each *vertical dotted line*, and many more bins compressed into the regimes where $\omega_{500} > 40$ and $\omega_{500} < -40$ hPa day^{-1}. NCEP relative humidity data above 300 mb are not available

anomalies at that same level seen in Fig. 4a. The GFDL model has a moister mid-troposphere and a dryer upper troposphere in the ascent regimes than CAM. The GMAO model is relatively moist throughout the troposphere. The reanalyses also disagree with each other significantly, particularly in the strong ascent regimes.

The cloud fraction, shown in Fig. 4c, also differs substantially between the models. In general CAM simulates higher cloud fraction than the other models, especially in the lower troposphere for almost all ω_{500} bins, and also near the tropopause in ascent regimes. The GFDL and GMAO models simulate less cloud cover below the 350 hPa level and a more vertically dispersed high cloud.

Figure 5 plots profiles of ω_{500}-binned grid-box-mean cloud liquid water, cloud ice and their sum, for which inter-model differences are large. Cloud liquid water content in CAM is quite large (>0.02 g kg^{-1} below the 900 hPa level) compared to boundary layer liquid water content in the other models. Even higher near-surface values (>0.04 g kg^{-1}) are found in CAM in the strong subsidence regimes. CAM also simulates a prominent peak of cloud liquid water in the ascent regimes just above the freezing level at around 500 hPa. In contrast the GFDL model has substantial cloud liquid water (>0.02 g kg^{-1}) spread between 800 and 600 hPa in the ascent regimes, and much more liquid water between 900 and 700 hPa in the subsidence regimes than the other models. In the GMAO model, cloud liquid water has a similar vertical and dynamical distribution pattern as in the GFDL model, but with liquid water contents typically less than half of those in the GFDL model. The ice water contents in Fig. 5b show more broad agreement between models (note the change of scale from liquid water), with all models having the highest ice contents between 400 and 200 hPa in strong ascent regimes. The peak ice water contents in CAM are in general much smaller than for the other models.

Figure 6 compares the model's integrated liquid water path over ocean with SSMI and TMI monthly averaged observations over ocean sorted by ECMWF ω_{500}. The SSMI and TMI measurements, which use the same retrieval algorithm but have different sensor footprint areas, are in fairly good agreement except in the strong ascent regimes, where TMI predicts a slightly lower LWP. All of the models have lower LWP than the satellite measurements in the strong subsidence regimes ($\omega_{500} > 30$ hPa day^{-1}). The GFDL model has significantly lower LWP in the strong ascent regimes ($\omega_{500} < -30$ hPa day^{-1}) than the satellite measurements, and the GMAO LWP is very low in all dynamical regimes. Because of potential biases in the satellite measurements, the comparisons with the models should be regarded with some caution.

When the models' water vapor paths over ocean are compared with SSMI observations (not shown), the agreement is satisfactory except in strong ascent regimes ($\omega_{500} < -30$ hPa day^{-1}) where the GFDL and CAM models have ~10% lower mean water vapor path than SSMI.

In summary, the GCM control simulations produce substantially different humidity, cloud cover, and con-

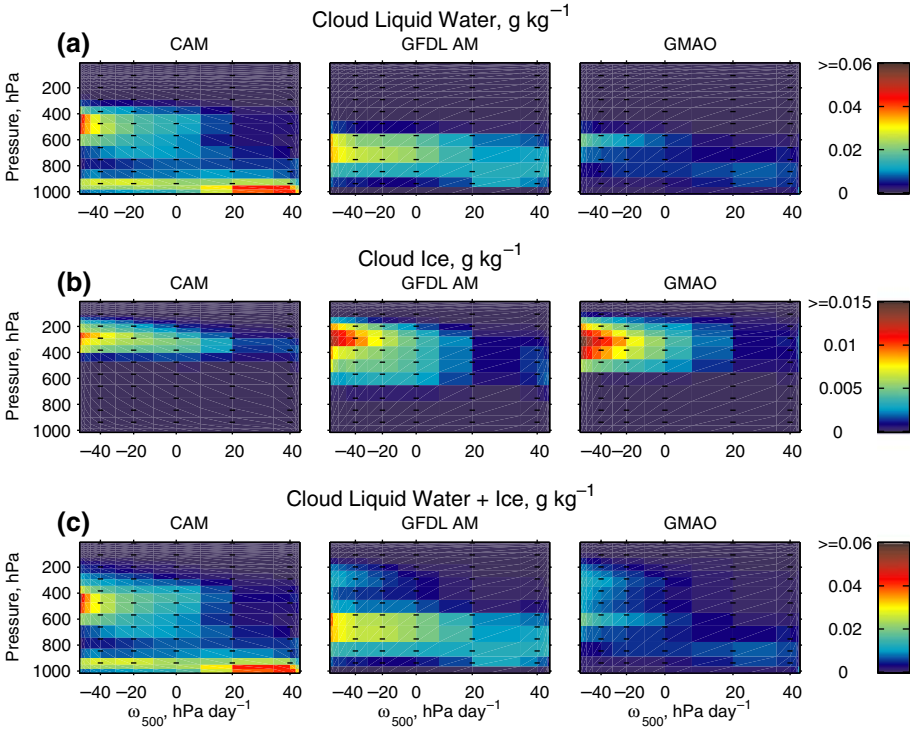

Fig. 5 **a** Cloud liquid water, **b** cloud ice, and **c** cloud liquid water and ice combined in g kg^{-1}, sorted by ω_{500} for the three GCMs

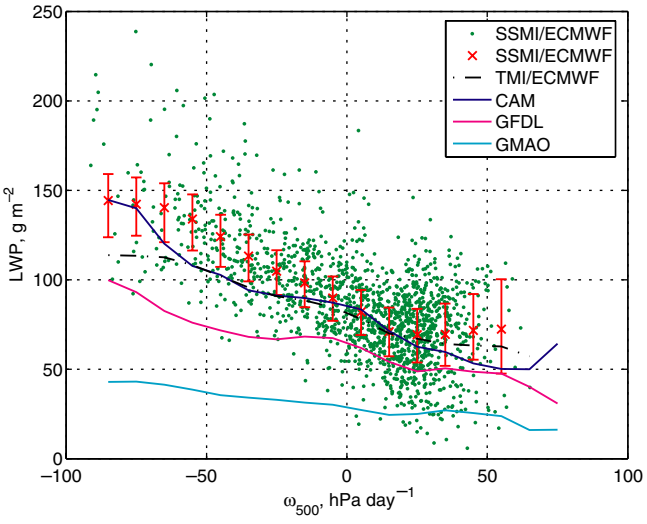

Fig. 6 Liquid water path over ocean as a function of pressure velocity. Monthly SSMI data are plotted as *green points* (6% of the points are plotted). The SSMI mean in each category is plotted with 25th and 75th percentile bars in *red*. Monthly TMI observations are plotted as a *broken black line*. The GCM means are plotted as *solid lines*

densate distributions, both with respect to height and dynamical regime. The good agreement of the models with ERBE cloud forcing across dynamical regimes is probably the natural result of constraining the GCM parameterizations to match the observed, present-climate TOA radiative fluxes.

5 Comparison with ISCCP data

To compare the models with satellite observations, we examine AMIP-style runs of the CAM and GFDL AM models. Both AMIP runs are forced with the same observed SSTs, but the model output we used was from slightly different periods, January 1984–December 2000 for CAM and January 1983–December 1998 for GFDL. Monthly climatologies of ISCCP simulator output from these runs are compared with a monthly climatology of the ISCCP data. The ISCCP D1 data extend from 1983 to 2001 (described in Sect. 2.1) and is sorted by monthly mean ECMWF ERA-40 ω_{500}.

The ω_{500} sorting is applied to cloud fraction in all seven ISCCP cloud-top pressure categories and in three optical depth (τ) ranges, thin ($0.02 \le \tau < 3.6$), intermediate ($3.6 \le \tau < 23$), and thick clouds ($\tau \ge 23$). The τ-sorted ISCCP cloud fraction is plotted in Fig. 7, as well as the sum over all optical thickness categories. Thin clouds (Fig. 7a) are a significant contributor to the total cloudiness at all heights and over the full ω_{500} range. They are especially prevalent in the upper troposphere in the ascent regimes, and also near the surface in the subsidence regimes. The latter category may be artificially enhanced by the aliasing of optically thicker subpixel scale cumulus clouds into the thin category. Intermediate thickness clouds (Fig. 7b) are prevalent in the same regimes as thin clouds, though the cloud fraction is relatively lower for moderate values of ω_{500}, and the high cloud in ascent regimes are concentrated a little lower, in the 180–310 hPa cloud-top pressure cat-

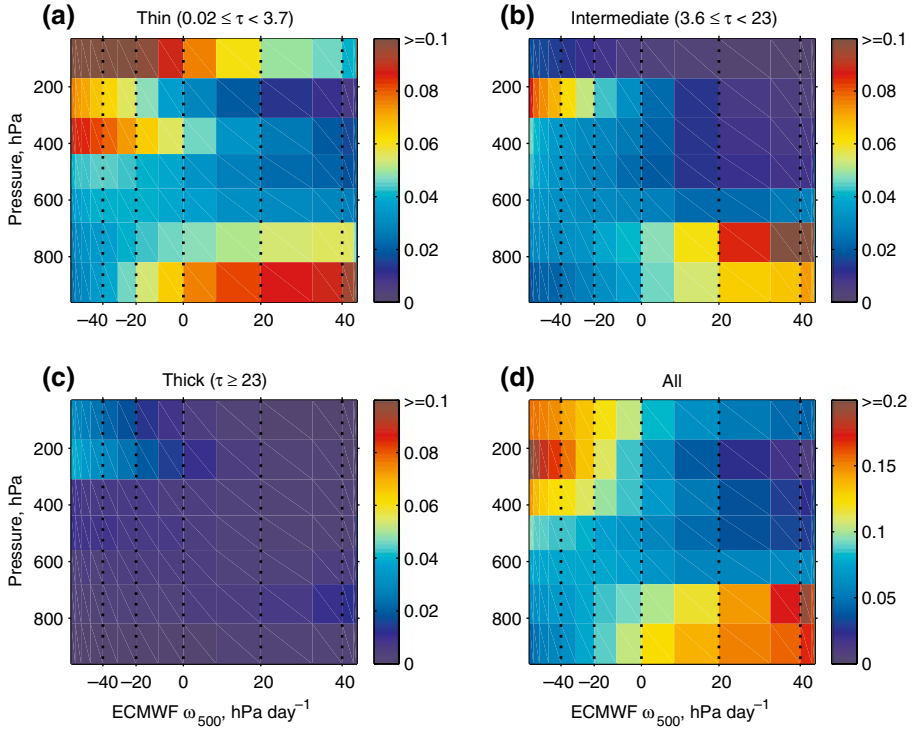

Fig. 7 ISCCP monthly mean cloud frequency sorted using the ω_{500} from ECMWF analysis, and divided into ISCCP cloud thickness categories: **a** thin ($0.02 \le \tau < 3.6$), **b** intermediate ($3.6 \le \tau < 23$), **c** thick ($\tau \ge 23$), and **d** all optical depths

egory. Thick clouds (Fig. 7c) are rare except near the tropopause in ascent regimes.

The CAM and GFDL τ-sorted cloud fractions are plotted in Figs. 8 and 9, respectively. The thinnest clouds ($\tau < 0.3$) have been deliberately excluded from the thin category (Figs. 8a and 9a) because these clouds are not reliably detected by ISCCP, even thought the thinnest ISCCP category nominally extends down to 0.02. Overall the model distributions in pressure and dynamical regime are qualitatively similar to each other, though CAM has almost universally higher cloud fraction than GFDL. Unlike in ISCCP, both CAM and GFDL thin clouds are found almost entirely in the uppermost cloud-top pressure bin, with the CAM thin cloudiness significantly over-predicted at all ω_{500}. At intermediate thicknesses the models have qualitatively the same pattern of cloud fraction as ISCCP, but both models (particularly GFDL) have less cloudiness in most categories than ISCCP. Both models have significantly more thick cloud than ISCCP data. CAM has significant thick boundary layer cloud that is not present in the GFDL model or the ISCCP data. CAM overestimates thick upper-tropospheric cloud, and the GFDL model overestimates thick mid-tropospheric cloud. The combined cloud fraction of CAM and GFDL is qualitatively similar to ISCCP, with the cloud found especially in the upper troposphere in ascent regimes, and the lower troposphere in subsiding regimes. However, the models underestimate clouds in other areas compared with ISCCP. The large discrepancies in overall cloud amount with height have been noted in Lin and Zhang (2004) and Zhang et al. (2005).

6 Response of the AGCMs to a +2K SST change

We now compare the response of the AGCMs to a +2K uniform SST increase following Cess et al. (1989, 1996). This perturbation illustrates the AGCM's response to a significant climate perturbation in a simple way, not requiring expensive multidecade simulations, yet retains salient characteristics of more realistic perturbations.

Figure 10a shows the PDF of ω_{500} for the CAM control case and the CAM +2K case. The +2K perturbation shows a slight overall weakening of the Hadley circulation, with reduction of the PDF at the extremes of the distribution and increase of the PDF between −30 and +20 hPa day^{-1}. A comparison of the change in PDF between the three GCMs (Fig. 10b) shows that this response to the uniform SST warming is typical, reflecting a negative (leftwards) shift of the PDF peak towards 0. This change multiplied by the mean cloud forcing in the control case is the dynamic term ($C\delta P$) in the B04 'budget.'

When we apply the B04 analysis to most variables of interest over the entire tropics, the integral of dynamic term across the ω_{500} PDF is small (< 20%) compared to the overall change, so we will be focusing on the thermodynamic term to understand the model response to climate perturbations. The relative contribution of the dynamic term for cloud forcing is particularly small (e.g., B04 and Table 4), and we will discuss this below.

The thermodynamic changes in temperature, relative humidity, grid-box-cloud fraction, and column-total cloud fraction from the +2K SST perturbation are

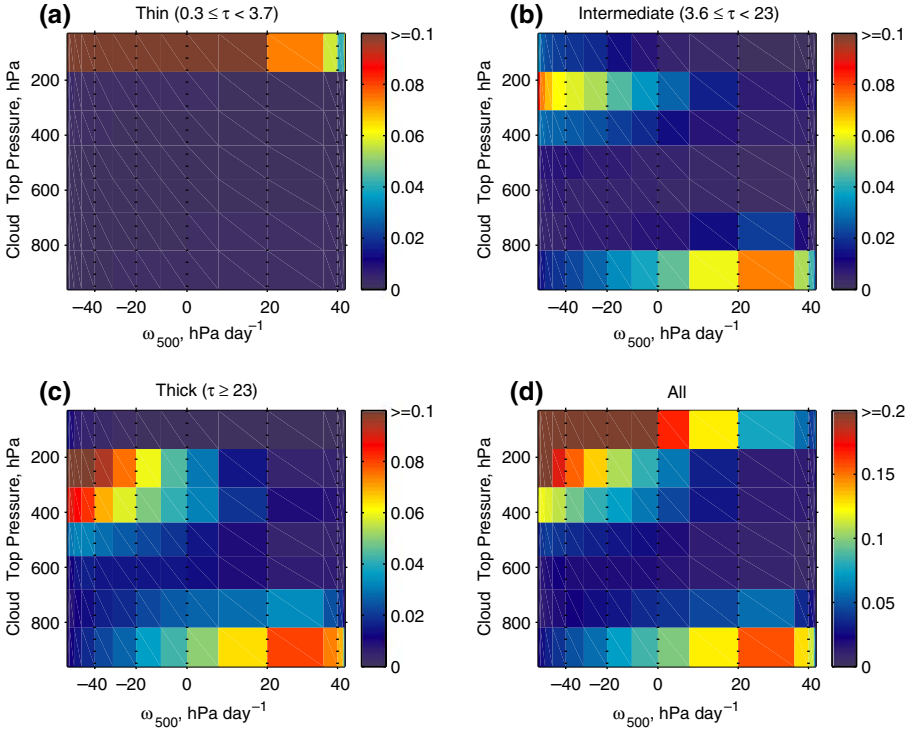

Fig. 8 CAM monthly mean cloud frequency from the ISCCP simulator for an AMIP run from 1984 to 2000 sorted by ω_{500} using thickness categories as in Fig. 7 except that the thin cloud category has a lower τ threshold of 0.3

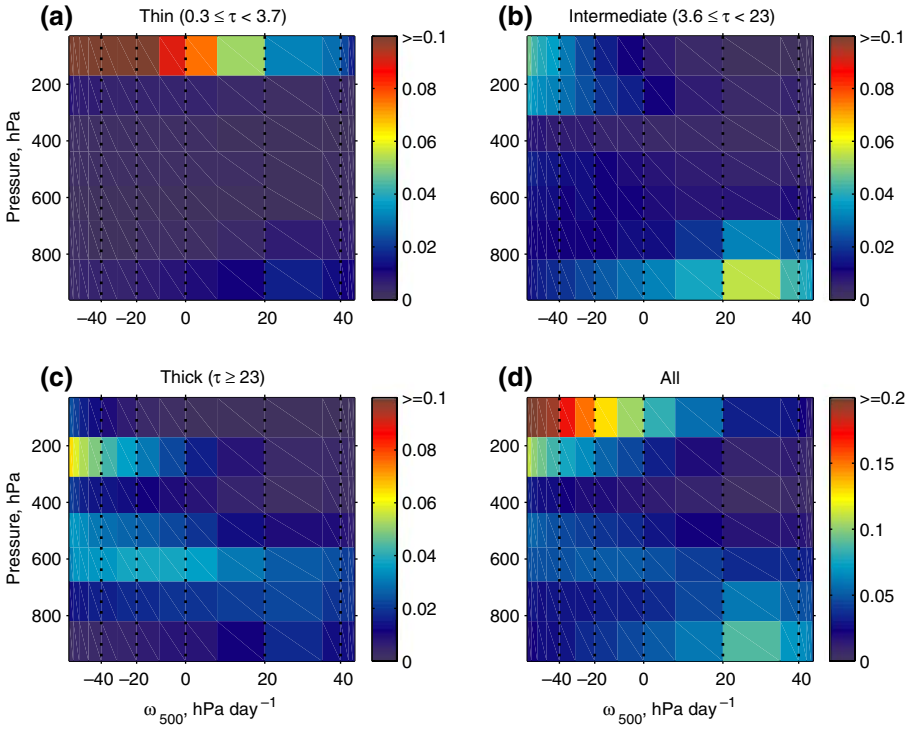

Fig. 9 GFDL AM monthly mean cloud frequency from the ISCCP simulator for an AMIP run from 1983 to 1998 sorted by ω_{500} using thickness categories as in Fig. 8

shown in Fig. 11. The upper tropospheric temperature responses of the models are broadly similar. All models show a 3–5 K warming of the upper troposphere in all ω_{500} bins driven by moist-adiabatic lapse rate feedback. The lower tropospheric temperature response differs more between the models. The relatively weak 1.5 K warming below the 750 hPa level in CAM contrasts with a 2–3 K warming in the GFDL and the GMAO models in this regime.

The models' relative humidity response to the +2K perturbation are diverse (Fig. 11b), especially in the ascent regimes. In the upper troposphere, the response of each model is partially (but not fully) explained with an upward shift of its mean RH profile corresponding to the upward shift of isotherms in the warmer climate. These model differences presumably reflect uncertainties in the parameterization of deep convection and cold cloud microphysics. Between 750 hPa and the surface, model RH changes are more closely connected with boundary layer and shallow convection parameterizations for all ω_{500} regimes. CAM has sizeable RH increases tied to the air temperature in this layer increasing less than the SST. The GMAO and GFDL models have only slight RH changes in this layer.

The +2K changes in cloud fraction (Fig. 11c, d) also differ substantially between the models. While all the models base their cloud fraction at least partially on RH, only CAM shows much correlation between cloud fraction and RH changes. In the upper troposphere much of the cloud fraction changes are dipoles associated with shifting upwards of the mean cloud fraction profile, especially in CAM and GFDL. GMAO has a broad reduction in cloud fraction despite significant zones of increasing RH. The changes in total column cloud fraction (Fig. 11d) reflect the dipole cancellation of cloud fraction changes in CAM and GFDL, but not in GMAO.

Figure 12 shows the response of the models' grid-box-mean cloud condensate to the +2K perturbation. Both cloud liquid water (Fig. 12a), and cloud ice (Fig. 12b), like cloud fraction, show significant dipole patterns associated with the shifting upward of condensate. The disagreement of the model condensate responses to the +2K perturbation is partly due to disagreements between the models' condensate in their respective control cases.

Other changes are model specific. In the ascent regimes, the GFDL model cloud liquid and ice increases substantially, which produces a huge net change in combined condensate path compared to the other models (Fig. 12c, d). In CAM there is a significant increase in cloud liquid water below 750 hPa across all ω_{500} bins associated with RH and cloud fraction increases. This is counteracted by a significant decrease in condensate in the layer immediately above.

The thermodynamic response to the change in longwave, shortwave, and net cloud forcing is shown in the top row of Fig. 13, normalized by the tropical mean surface temperature change. The change in cloud forcing to the +2K SST perturbation is quite varied between the three models. The CAM runs show a weak negative change in LWCF and SWCF due to significant vertical cancellation of changes in cloud fraction and condensate path. In the ascent regimes, the GFDL model has large strengthening of LWCF and SWCF (more strongly negative SWCF) associated with large increases in

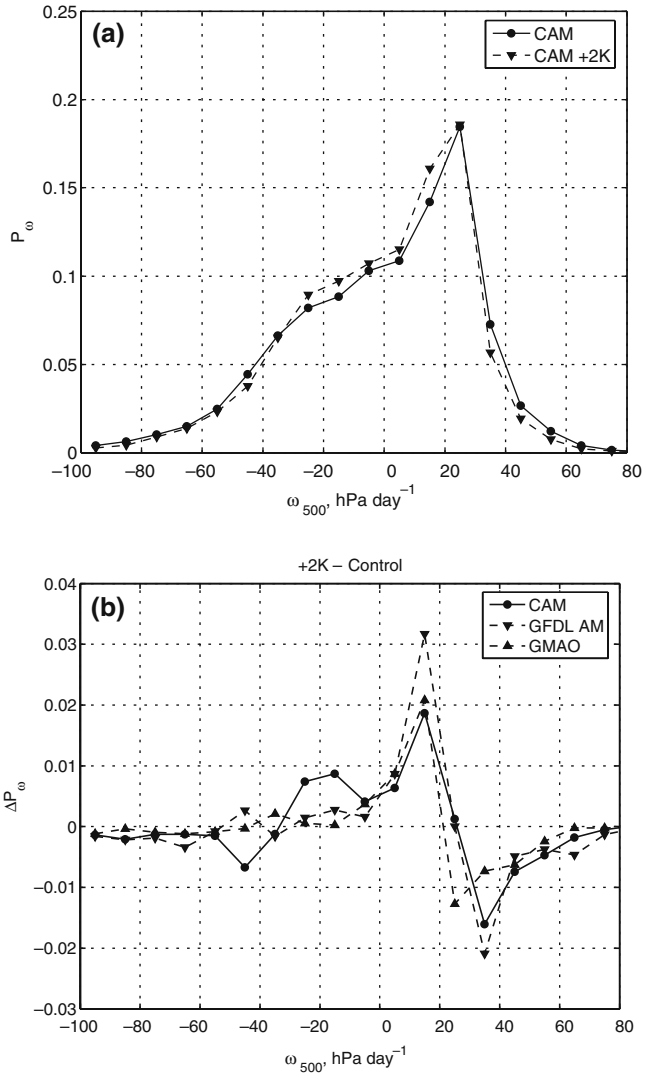

Fig. 10 **a** The ω_{500} PDF for the CAM +2K case and the CAM control case. **b** The change in normalized ω_{500} PDF between the +2K perturbation case and the control case for the three GCMs

condensate path. By contrast, in the subsidence regimes the SWCF weakens substantially (becomes less negative) due to a substantial decrease in cloud fraction. The net cloud forcing is primarily positive. The GMAO model exhibits strong weakening of SWCF and LWCF associated with large decreases in cloud fraction and small decreases in condensate path across all ω_{500} bins, with the SWCF weakening dominating the net cloud forcing.

Table 4 gives the breakdown of LWCF, SWCF, and net cloud forcing into thermodynamic ($P\delta C$) dynamic ($C\delta P$), and co-variation ($\delta P\delta C$) terms from Eq. 4 summed over all ω bins. The net cloud forcing due to the +2K change is -1.49 W m^{-2} for CAM, 1.00 W m^{-2} for GFDL AM, and 2.78 W m^{-2} for the GMAO model, dominated by the thermodynamic term. The only variable where the thermodynamic term does not dominate the overall change is the SWCF in the GFDL AM model. However, the dynamic term and the co-variation term are quite small in this case as well, so the overall change in SWCF is only 0.08 W m^{-2}.

The dynamic term for LWCF and SWCF and for most climate variables is quite large for individual ω_{500} bins. That the dynamic term is still small when summed over all ω_{500} bins, as in Table 4 and B04, is actually quite remarkable, and certainly not guaranteed by the construction of the diagnostic.

It is useful to consider the size of the summed dynamic term for an idealized control variable C_ω that is a linear function of ω and two constants: $C_\omega = C_0 + C_1\omega$. Reverting to the continuous definition of the dynamic term from B04, and substituting for C_ω, the dynamic term is

$$\int C_\omega \delta P_\omega \mathrm{d}\omega = \int C_0 \delta P_\omega \mathrm{d}\omega + \int C_1 \omega \delta P_\omega \mathrm{d}\omega. \tag{7}$$

The first term on the right-hand side is identically zero by the normalization condition of P_ω. So the dynamic term is equal to the second term, which is just $C_1\overline{\delta\omega}$, where $\overline{\delta\omega}$ is the domain averaged change in ω. If $\bar{\omega} = 0$ in a given domain for both the control and perturbed climates, the dynamic term would vanish. In reality this is nearly but not exactly true. In the case of LWCF and SWCF we can estimate C_1 by fitting a line to the left part of the control case values (from Fig. 3a, b). For the CAM +2K case, $\overline{\delta\omega} = -0.23$ hPa day^{-1},

Table 4 The size of the terms in the Bony analysis of the change in cloud forcing in W m^{-2} between the +2K run and the control run for the three GCMs

Model	Term	Longwave CF	Shortwave CF	Net CF
CAM	Mean	31.61	−55.90	−24.29
	Thermodynamic	−0.84	−0.50	−1.34
	Dynamic	−0.03	0.02	−0.01
	Co-variation	−0.07	−0.07	−0.14
	Mean change	−0.94	−0.55	−1.49
GFDL AM	Mean	26.25	−56.08	−29.83
	Thermodynamic	1.00	0.01	1.01
	Dynamic	−0.09	0.04	−0.05
	Co-variation	0.01	0.03	0.04
	Mean change	0.92	0.08	1.00
GMAO	Mean	36.81	−54.64	−17.83
	Thermodynamic	−2.22	4.86	2.64
	Dynamic	0.10	0.08	0.18
	Co-variation	−0.03	−0.01	−0.04
	Mean change	−2.15	4.93	2.78

The mean change in net cloud forcing is dominated by the thermodynamic term

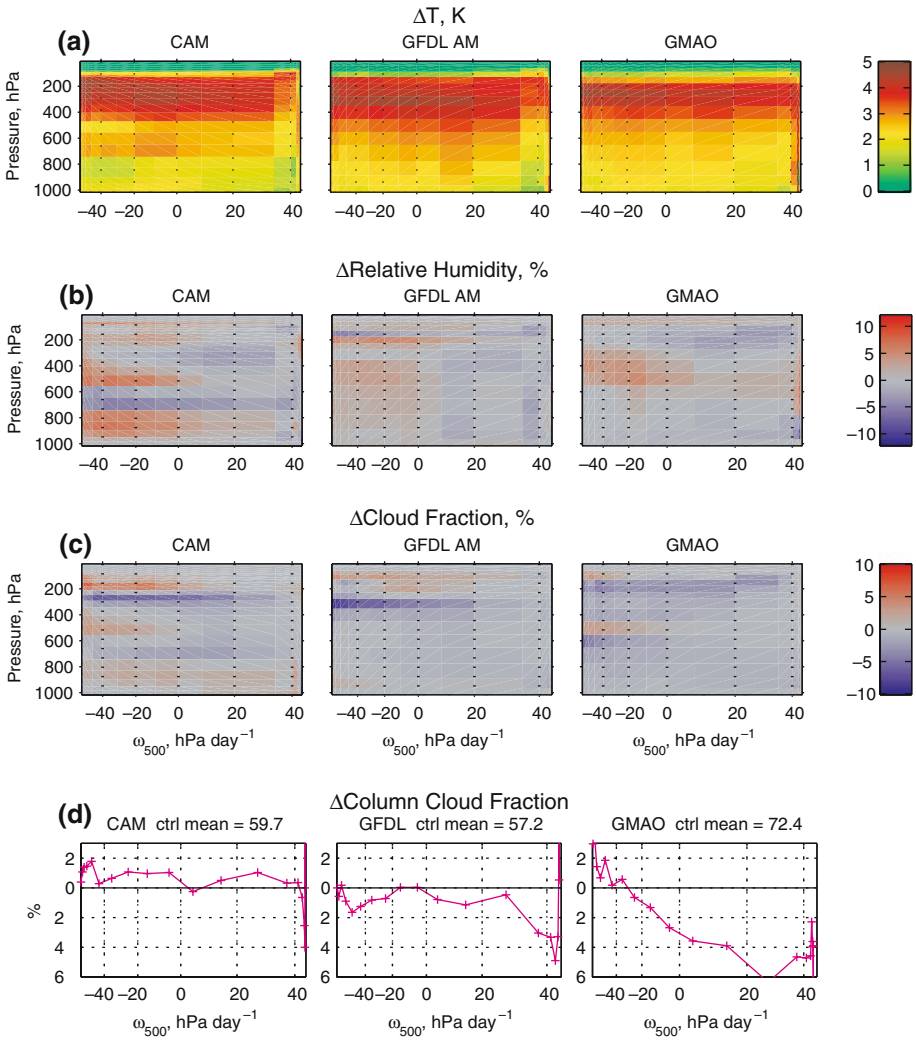

Fig. 11 The change in **a** temperature (K), **b** relative humidity (%), **c** cloud fraction, and **d** column-integrated cloud fraction between the +2K case and the control case for the three GCM models. Since the *x*-axis is stretched, the area average of the change at a given level is proportional to the thermodynamic term in the Bony analysis, $P\delta C$

$C_{1\mathrm{LWCF}} \approx -0.8$, and $C_{1\mathrm{SWCF}} \approx +0.8\,\mathrm{W\,m^{-2}\,hPa^{-1}\,day}$, so the estimated dynamic term for LWCF is $+0.2$ W m^{-2} and for SWCF -0.2 W m^{-2}, as compared to the actual terms -0.03 and $+0.02$ W m^{-2}, respectively. Thus the actual dynamic terms are much smaller in magnitude than expected from a simple linear fit. We think this pattern is coincidental, but it also holds for the cloud forcing for other models' +2K runs.

A key question in applying a regime-sorting approach to climate change is whether the climate change response in some variable C (e.g., SWCF) in individual locations and months can be well predicted from the mean thermodynamic response δC_ω of their regime. If so, the regime-sorting provides an economical summary of the time and space dependent climate response. If not, the regime-sorted response may merely be the amalgam of various regionally specific responses with disparate causes.

We approach this question by computing climate change responses δC^{col} and $\delta\omega_{500}^{\mathrm{col}}$ in individual column-months. We partition δC^{col} into a dynamic and a residual component. The dynamic component is $\delta C_{\mathrm{dyn}}^{\mathrm{col}} = \delta\omega_{500}^{\mathrm{col}}(\partial C_\omega/\partial\omega)$, where the rightmost factor is the approximate slope of C_ω in the control climatology (e.g., from Fig. 3) evaluated at the ω_{500} value of the particular column-month. The residual component $\delta C_{\mathrm{res}}^{\mathrm{col}} = \delta C^{\mathrm{col}} - \delta C_{\mathrm{dyn}}^{\mathrm{col}}$ of all column-months can then be sorted by ω_{500} and compared with the regime-sorted thermodynamic change δC_ω. By construction, the mean of $\delta C_{\mathrm{res}}^{\mathrm{col}}$ over all column-months in the bin should closely match δC_ω; it is the relative magnitude of the scatter of $\delta C_{\mathrm{res}}^{\mathrm{col}}$ about this mean that we are interested in here.

For example, let C be GMAO SWCF and consider the +2K climate perturbation. Figure 14 shows the $\omega_{500}^{\mathrm{col}}$-binned mean and standard deviation of $\delta C_{\mathrm{res}}^{\mathrm{col}}$ about this mean over all column-months. Comparison of Fig. 14 with the actual thermodynamic term in Fig. 13 verifies that the mean $\delta C_{\mathrm{res}}^{\mathrm{col}}$ indeed closely matches the thermodynamic contribution δC_ω. For the column-months with mean subsidence, especially for $\omega_{500}^{\mathrm{col}}$ between +20 and +30 hPa day^{-1}, the regime-mean $\delta C_{\mathrm{res}}^{\mathrm{col}}$ is roughly 1 standard deviation, indicating that around half of the mean square $\delta C_{\mathrm{res}}^{\mathrm{col}}$ in column-months in these bins can be explained by the regime-averaged δC_ω. This was chosen as a particularly favorable case; for most models and fields, a more modest (though usually sta-

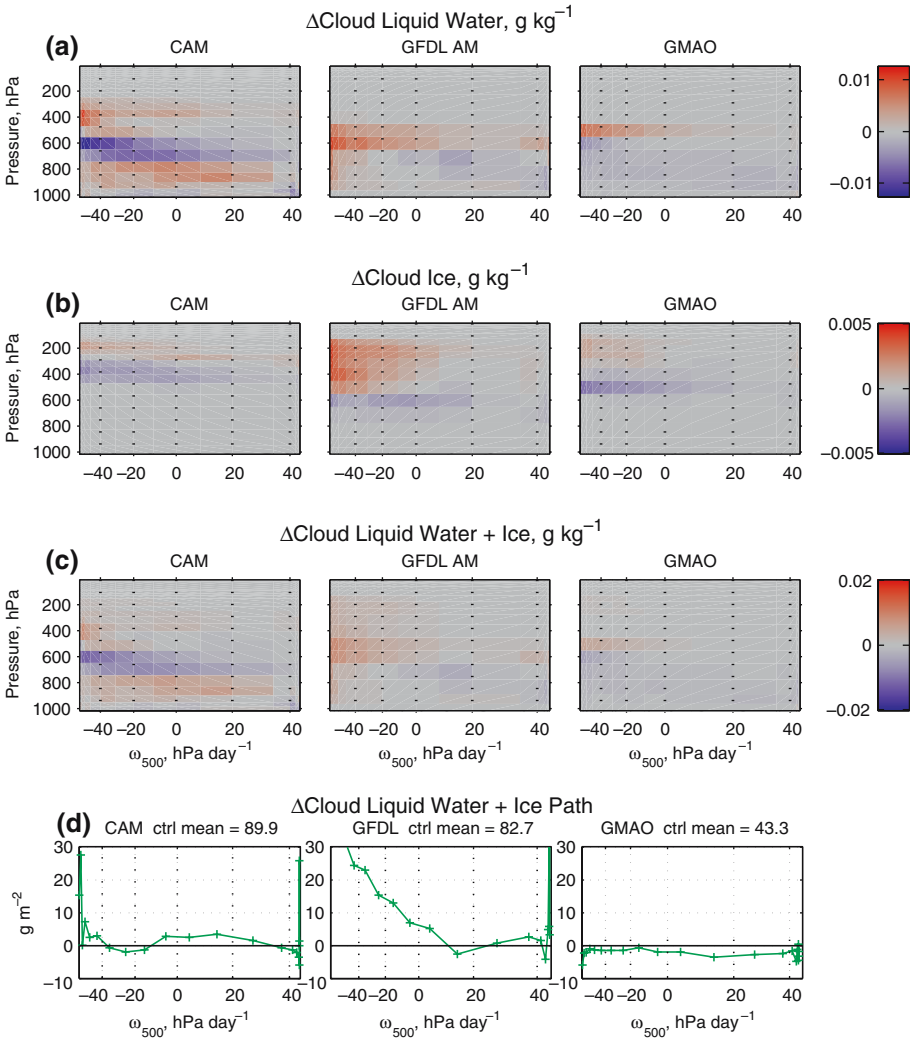

Fig. 12 As in Fig. 11, but for cloud liquid water, cloud ice, and cloud liquid water + ice in g kg^{-1}, and liquid + ice path in g m^{-2}

tistically significant) fraction of the column residual changes are explainable by regime-sorting. Thus, the Bony approach is useful for diagnosis of climate perturbations, but is less skillful for this purpose than it is for rationalizing the space–time variability of low-latitude clouds in the current climate.

The dynamic component $\delta C^{\mathrm{col}}_{\mathrm{dyn}}$ also contributes substantially to δC^{col}. For our example it explains 50–70% of the mean-square δC^{col} in the ascent regimes (because of changes in the location and intensity of the tropical rainfall belts), though it is much less variable than the residual component in most of the subsidence regime (not shown). Interpretation of climate change in fixed geographic regions is a necessary complement to ω_{500} regime-sorting but must not ignore the possibly large dynamic component of any cloud changes.

7 Response to other climate perturbations

Now we investigate the effects of alternate types of climate perturbations on cloud properties and cloud forcing. In addition to a +2K SST change, we also consider a −2K change, the ΔCMIP SST change, and doubling of CO_2 in simulations with a slab-ocean model. Not all climate perturbation types were performed all of the models. Note that we define the response in the −2K perturbation case as control minus −2K.

Figure 15 shows the annual-mean ΔSST (SST perturbation) patterns for the ΔCMIP and 2×CO_2 climate perturbations. For the ΔCMIP case (Fig. 15a), ΔSST is everywhere positive, but less than 2K and weaker south of the equator, particularly off the west coast of South America. Figure 15b, c shows the mean annual SST changes in the CAM and GFDL runs for the 2×CO_2 case, respectively. The CAM ΔSST (Fig. 15b) has a narrow local maximum of ΔSST near the Pacific ITCZ and relatively weak ΔSST in the Atlantic north of the equator. The GFDL model SST pattern is very similar to the ΔCMIP perturbation, but with 50% higher amplitude SST perturbations. These two different ΔSST patterns of CAM and GFDL partially reflect the feedback of their different cloud responses to the CO_2 increase. The mean amplitudes of both the 2×CO_2 SST responses are larger than the specified ΔCMIP SST perturbation primarily because the former simulations

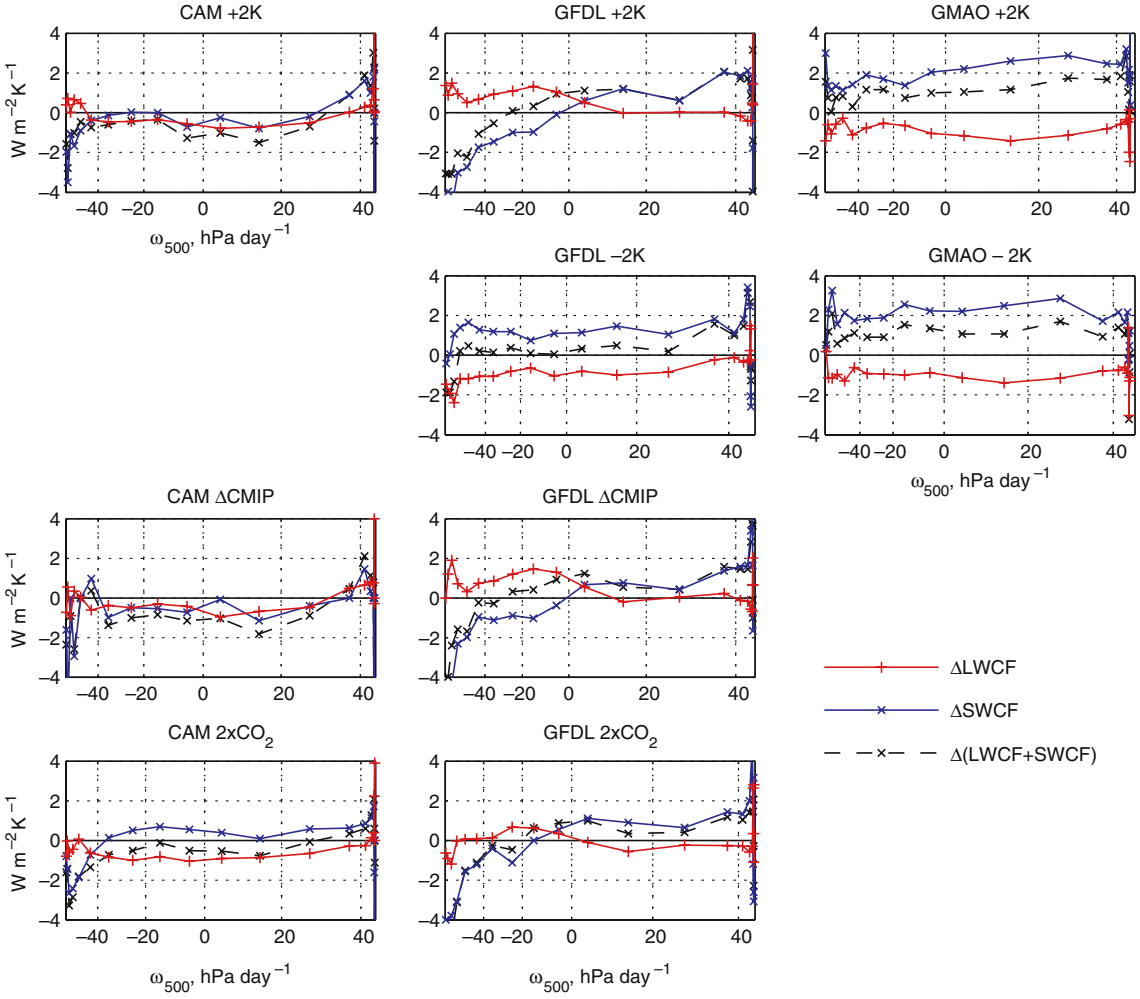

Fig. 13 The change in LWCF (*red*), SWCF (*blue*), and net cloud forcing (*black*) normalized by the tropical mean change in surface temperature, in W m^{-2} K^{-1}, as a function of ω_{500} for various simulations compared with the control simulations. The 2×CO_2 plot is the difference of the 2×CO_2 run from the 1×CO_2 control run. The *x*-axis is stretched in proportion to the control run ω_{500} PDF

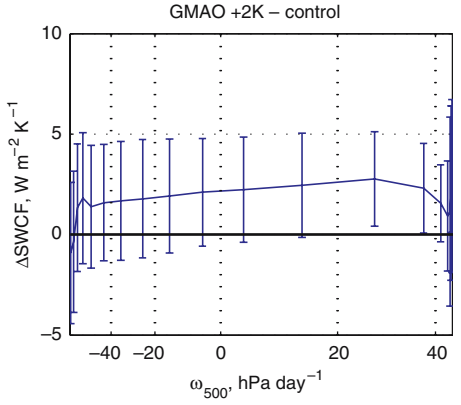

Fig. 14 The fixed column-month mean SWCF changes as a function of ω_{500} for the GMAO +2K perturbation with estimated dynamic contribution removed, $\delta C_{\mathrm{res}}^{\mathrm{col}}$, normalized by the mean surface temperature change. The *bars* indicate the standard deviation from the mean

are close to equilibrium, while the coupled CMIP models were not.

The thermodynamic terms for cloud forcing for all of the climate experiments are plotted in Fig. 13. Also plotted in Fig. 16 are the tropics-wide total changes of cloud fraction, ice + liquid water condensate path, and shortwave, longwave, and net cloud forcing for all the climate perturbation experiments. Low, middle, and high cloud fraction and condensate path categories differ slightly by model: CAM low, middle, and high categories are divided at 700 and 400 hPa, GFDL at 680 and 440 hPa, and GMAO at 700 and 500 hPa. Cloud fraction is calculated using the individual models' overlap methods and does not involve the ISCCP simulator. To simplify the comparisons, both Figs. 13 and 16 are normalized by the mean surface temperature change.

Each model shows a qualitative consistency of response across most perturbation types. This can be seen in the LWCF and SWCF thermodynamic term profiles

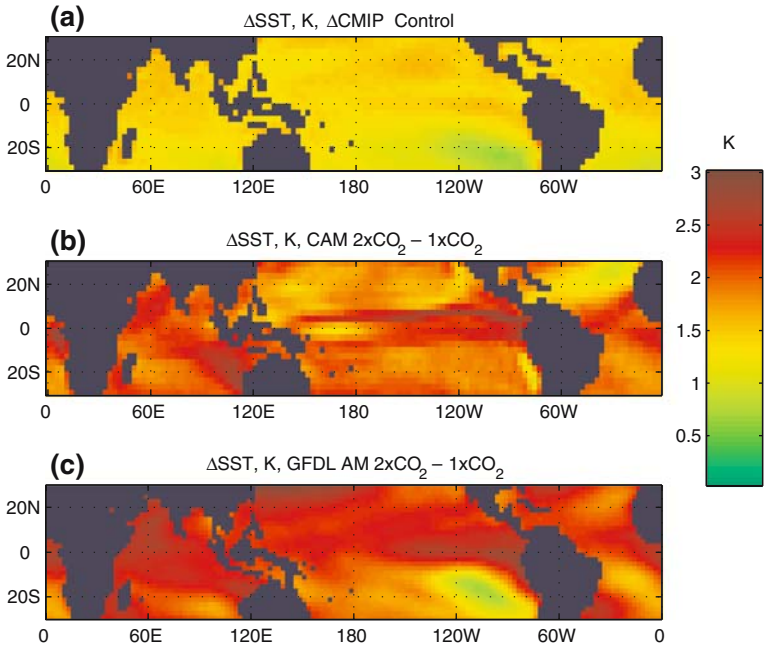

Fig. 15 Mean annual SST difference between **a** *Δ*CMIP and the control run, **b** CAM $2\times CO_2$ run and $1\times CO_2$ run, and **c** GFDL AM $2\times CO_2$ run and $1\times CO_2$ run

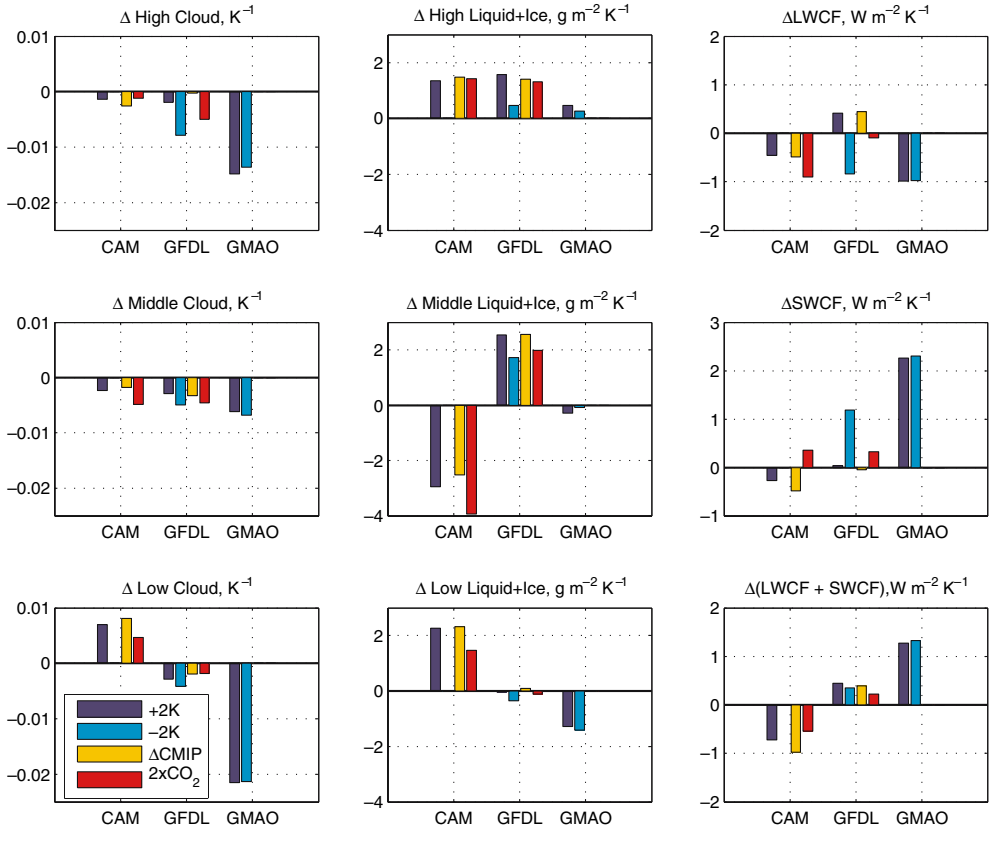

Fig. 16 Changes in cloud amount (K^{-1}), ice + liquid water path (g m^{-2} K^{-1}), LWCF, SWCF, and net cloud forcing (W m^{-2} K^{-1}), normalized by tropical mean surface temperature change, for all the perturbation types: +2K, −2K, *Δ*CMIP, and $2\times CO_2$. Note that there are no runs for the following cases: CAM −2K, GMAO *Δ*CMIP, and GMAO $2\times CO_2$

(Fig. 13), and in tropical mean response of cloud fraction, condensate amount, and net cloud forcing (Fig. 16). However, there are a few significant differences, as discussed below.

The most similar case to the uniform +2K perturbation is the ΔCMIP case, performed for CAM and GFDL, which involves a SST forcing pattern that is mostly flat. The LWCF and SWCF changes (Fig. 13, third row) and cloud fraction and condensate path changes (Fig. 16) are very similar to the +2K case for both CAM and GFDL.

The $2\times CO_2$ case varies significantly from the +2K case for both CAM and GFDL, but in different ways for each model. For the CAM $2\times CO_2$ perturbation, ΔSWCF is positive from −40 to +30 hPa day^{-1}, while in the +2K case it is negative or zero. A large part of this difference is caused by a disparity in low cloud response. The $2\times CO_2$ case has less boundary layer RH increase from 0 to 40 hPa day^{-1} and less increase in low cloud fraction across dynamic regimes (not shown). The CAM $2\times CO_2$ perturbation also has a slightly stronger decrease in LWCF compared to the +2K case, due to a stronger decrease in middle cloud amount and condensate path. The net result of doubling CO_2 is a negative cloud forcing, but less so than for the +2K perturbation.

In the case of GFDL, it is the ascent regimes where the $2\times CO_2$ differs from the +2K case. The middle and high cloud fraction decrease more in the $2\times CO_2$ case, and the middle and high condensate path increase less. Both factors increase SWCF and lower LWCF in the ascent regimes, the net effects of which largely cancel.

We expect the response in the GMAO and GFDL −2K perturbation experiments (defined as control minus −2K) to be similar to their respective +2K perturbation responses. This is true for GMAO but not for GFDL. In the GFDL −2K case, the large cumulative increase in condensate for warmer SST in ascent regimes that is seen in the +2K response is much reduced. The −2K case also has stronger reduction in middle and high cloud fraction. This causes a large decrease in SWCF and increase in LWCF for all negative omegas. Experiments with the Tokioka entrainment rate limiter removed (not shown) do not have this strong asymmetry.

8 Discussion and conclusions

As found by B04, the ω_{500}-sorted model LWCF and SWCF in all three AGCM models studied here agree well with ERBE observations. This agreement hides a number of significant underlying differences in the models' representation of clouds and cloud processes. The disparate responses of LWCF and SWCF in the models to identical climate perturbations further expose these differences between the models.

The liquid water path is underestimated substantially in the GFDL and GMAO models, particularly in the ascent regimes, compared to satellite microwave estimates sorted by reanalysis ω_{500}. That their SWCF profiles are so similar shows how strongly other factors, such as parameterization of cloud fraction and cloud overlap assumptions can compensate for this bias. The mean vertical profiles of temperature and relative humidity in CAM have substantially more complicated vertical structure in the ascent regimes than the other models or reanalysis. The CAM temperature, humidity, condensate, and cloud fraction responses in the ascent regimes to the +2K perturbation appear to be substantially related to this structure.

Model simulated low clouds in the subsidence regimes also show huge differences between models. CAM has unrealistically large low cloud fractions over a broad range of dynamical regimes. It has very large liquid water contents below 950 hPa over the oceans, especially in subtropical stratocumulus regimes. This may be due to CAM's surface-forced boundary layer scheme (Holtslag and Boville 1993) that does not include the effects of stratocumulus cloud-top cooling in enhancing entrainment rate, causing an unrealistically shallow boundary layer. The GFDL scheme, based on Lock et al. (2000), which contains more detailed marine boundary layer physical processes, under-predicts low cloud fraction substantially in the subtropical stratocumulus regions (GAMDT 2004). The GFDL model also has unusually high mean condensate up to 550 hPa in the subsidence regimes injected by sporadic cumulus convection.

In the climate perturbation experiments, the low cloud amount and low cloud fraction responses are consistent between perturbation types but quite different between models (CAM increases both, GFDL decreases both, and GMAO sharply decreases both), reflecting continuing uncertainty in boundary layer cloud parameterization. The tropics-wide differences TOA net cloud forcing can be largely explained by differences in low cloud (Fig. 16, bottom row) as the substantial inter-model differences in upper and especially middle level clouds appear to largely cancel.

In the ascent regimes there are two significant unexplained results of the climate experiments. One is the strong increase in condensate at mid-levels in GFDL due to a warming climate perturbation, compared with a strong condensate decreases in CAM at mid-levels. The other is the asymmetry of the response of the GFDL AM between SST perturbations of +2K and −2K.

The substantial differences in clouds and especially cloud responses in ascent regimes are surprising given the underlying similarity between the deep-convective schemes of the models. The GMAO and GFDL models both use RAS schemes, and CAM scheme uses the mass flux scheme of Zhang and McFarlane (1995), which itself is based on an Arakawa–Schubert-like ensemble of entraining plumes. The regime-sorted differences between the GMAO and GFDL condensate profiles show how sensitive the model clouds are to microphysical assumptions and internal RAS parameters. For instance, two important differences between the two

models' RAS implementations are: (1) the fraction of parameterized updraft condensate that is converted to precipitation, which controls the amount of detrained moisture, and (2) GFDL's use of a Tokioka entrainment rate limiter, preventing undiluted cumulus updrafts. Sensitivity tests show that this limiter may partly account for the overall lower cloud fraction of GFDL relative to the other models.

Comparison of CAM and GFDL models with the ISCCP simulator sorted by ω_{500} highlights some common problems shared by GCMs including over-predicting thick clouds and high thin clouds and under-predicting other thin clouds and mid-level-top clouds, in agreement with other studies. The limited vertical resolution of modern operational GCMs likely inhibits accurate prediction of thin clouds. However this is clearly not the only problem, as higher resolution runs of some of these models still produce large cloud biases. Even with much higher vertical resolution, adequate parameterization of both shallow and deep convection must still redistribute heat and moisture accurately in order to simulate cloudiness well.

The B04 method provides a useful method for isolating biases in the models as well as illuminating the strong model differences of clouds due to climate perturbations. The relative importance of the geographically dominant weak-subsidence regimes is highlighted, and the complicating effects of dynamic perturbations are largely separated out for most variables of interest. One shortcoming of the approach is that regime-sorting only explains a limited fraction of the residual variance of the climate change response of many cloud-related variables in individual column-months after dynamical effects have been removed. Regional factors such as nearby land or ocean surface type and local advective effects must still be scrutinized to understand the overall climate response. Further, for analyzing climate perturbations of the simple types presented here, the B04 method is limited to comparison between models as there are no direct observations to compare with.

An important next step is to try to better understand some of the substantial differences between models discussed above under conditions of similar dynamic forcing. One possible approach is to use the ω_{500}-sorted GCM output as forcing for single-column versions of the GCMs and cloud-resolving models. Continuing development of cloud-related observational data sets is also essential to making progress in representing clouds in large-scale models.

Acknowledgments This paper grew out of a multi-institution Climate Process Team whose goal is to reduce the uncertainty in representing low-latitude cloud feedbacks on climate change by improving the representation of cloud processes in GCMs (Bretherton et al. 2004). The authors would like to thank Cecile Hannay, Jim Mccaa, Christine Shields at NCAR for their assistance with CAM and the CAM simulations, Paul Kushner, Rich Gudgel, and Tom Knutson for producing some of the GFDL simulations. Also thanks to Mark Stevens at NCAR for gridding the NCEP, SSMI, and ERBE data. Thanks to Rob Wood for the providing processed monthly TMI data, Peter Blossey for helpful discussions, and Marc Michelson for computer support. The authors thank Edwin Schneider and several anonymous reviewers who helped improve this paper. SSMI data are produced by Remote Sensing Systems and sponsored by the NASA Earth Science REASoN DISCOVER Project. Data are available at http://www.remss.com. ERA-40 data were provided by ECMWF. Funding for this work was provided by NSF grant 0336703 and NOAA by the Joint Institute for the Study of the Atmosphere and Ocean (JISAO) under NOAA Cooperative Agreement No. NA17RJ1232, Contribution, #1153.

References

Bony S, Dufresne J-L, Le Treut H, Morcrette J-J, Senior C (2004) On dynamic and thermodynamic components of cloud changes. Clim Dyn 22:71–86

Bretherton CS, Ferrari R, Legg S (2004) Climate process teams: a new approach to improving climate models. US CLIVAR Variations 2(1):1–6

Cess RD et al (1989) Interpretation of cloud-climate feedback as produced by 14 atmospheric general circulation models. Science 245:513–516

Cess RD et al (1996) Cloud feedback in atmospheric general circulation models: an update. J Geophys Res 101:12791–12794

Charlock TP, Ramanathan V (1985) The albedo field and cloud radiative forcing produced by a general circulation model with internally generated cloud optics. J Atmos Sci 42:1408–1429

Chen C, Cotton WR (1987) The physics of the marine stratocumulus-capped mixed layer. J Atmos Sci 44:2951–2977

Collins WD, Rasch PJ, Boville BA, Hack JJ, McCaa JR, Williamson DL, Kiehl JT, Briegleb B, Bitz C, Lin S-J, Zhang M, Dai Y (2004) Description of the NCAR Community Atmosphere Model (CAM 3.0). NCAR Technical Note, NCAR/TN-464 + STR, 226 pp

Del Genio AD, Yao MS, Kovari W, Lo K-W (1996) A prognostic cloud water parameterization for global climate models. J Clim 9:270–304

The GFDL Global Atmospheric Model Development Team (2004) The new GFDL global atmosphere and land model AM2–LM2: evaluation with prescribed SST simulations. J Clim 17:4641–4673

Hack JJ (1994) Parameterization of moist convection in the National Center for Atmospheric Research Community Climate Model (CCM2). J Geophys Res 99:5551–5568

Harrison EF, Minnis P, Barkstrom BR, Ramanathan V, Cess RD, Gibson GG (1990) Seasonal variation of cloud radiative forcing derived from the earth radiation budget experiment. J Geophys Res 95:18687–18703

Holtslag AAM, Boville BA (1993) Local versus nonlocal boundary-layer diffusion in a global climate model. J Clim 6:1825–1842

Kalnay E et al (1996) The NCEP/NCAR 40-year reanalysis project. Bull Am Meteorol Soc 77:437–471

Kiehl KT, Ramanathan V (1990) Comparison of cloud forcing derived from the earth radiation budget experiment with that simulated by the NCAR community climate model. J Geophys Res 95:11679–11698

Klein SA, Hartmann DL (1993) The seasonal cycle of low stratiform clouds. J Clim 6:1587–1606

Klein SA, Jakob C (1999) Validation and sensitivities of frontal clouds simulated by the ECMWF model. Mon Weather Rev 125:2514–2531

Lin WY, Zhang MH (2004) Evaluation of clouds and their radiative effects simulated by the NCAR community atmospheric model CAM2 against satellite observations. J Clim 17:3302–3318

Lin YL, Farley RR, Orville HD (1983) Bulk parameterization of the snow field in a cloud model. J Clim Appl Meteorol 22:1065–1092

Lock AP, Brown AR, Bush MR, Martin GM, Smith RNB (2000) A new boundary layer mixing scheme. Part I. Scheme description and single-column model tests. Mon Weather Rev 128:3187–3199

Louis JM, Tiedtke M, Geleyn J (1982) A short history of the PBL parameterization at ECMWF. In: Proceedings of ECMWF workshop on planetary boundary layer parameterization, Reading, UK, pp 59–80

Meehl GA, Boer GJ, Covey C, Latif M, Stouffer RJ (2000) The coupled model intercomparison project (CMIP). Bull Am Meteorol Soc 81:313–318

Moorthi S, Suarez MJ (1992) Relaxed Arakawa–Schubert: a parameterization of moist convection for general circulation models. Mon Weather Rev 120:978–1002

Rasch PJ, Kristjansson JE (1998) A comparison of the CCM3 model climate using diagnosed and predicted condensate parameterizations. J Clim 11:1587–1614

Rayner NA, Parker DE, Horton EB, Folland CK, Alexander LV, Rowell DP, Kent EC, Kaplan A (2003) Global analyses of sea surface temperature, sea ice, and night marine air temperature since the late nineteenth century. J Geophys Res 108(D14):4407. DOI 10.1029/2002JD002670

Reynolds RW, Smith TM (1994) Improved global sea surface temperature analyses using optimum interpolation. J Clim 7:929–948

Rossow WB, Schiffer RA (1999) Advances in understanding clouds from ISCCP. Bull Am Meteor Soc 80:2261–2287

Rotstayn LD (1997) A physically based scheme for the treatment of stratiform clouds and precipitation in large-scale models. I. Description and evaluation of microphysical processes. Q J R Meteorol Soc 123:1227–1282

Rotstayn LD, Ryan BF, Katzfey J (2000) A scheme for calculation of the liquid fraction in mixed-phase clouds in large-scale models. Mon Weather Rev 128:1070–1088

Senior CA, Mitchell JFB (1996) Carbon dioxide and climate: the impact of cloud parameterization. J Clim 6:393–418

Smith GL, Wielicki BA, Barkstrom BA, Lee RB, Priestley KJ, Charlock TP, Minnis P, Kratz DP, Loeb N, Young DF (2004) Clouds and earth radiant energy system: an overview. Adv Space Res 33:1125–1131

Soden B, Broccoli AJ, Hemmler RS (2004) On the use of cloud forcing to estimate cloud feedback. J Clim Lett 17:3661–3665

Sud YC, Walker GK (1999) Microphysics of clouds with the relaxed Arakawa–Schubert scheme (McRAS). Part I. Design and evaluation with GATE Phase III data. J Atmos Sci 56:3196–3220

Tiedtke M (1993) Representation of clouds in large-scale models. Mon Weather Rev 121:3040–3061

Tokioka T, Yamazaki K, Kitoh A, Ose T (1988) The equatorial 30–60 day oscillation and the Arakawa–Schubert penetrative cumulus parameterization. J Meteorol Soc Jpn 66:883–901

Trenberth KE, Caron JM (2001) Estimates of meridional atmosphere and ocean heat transports. J Clim 14:3433–3434

Uppala SM et al (2005) The ERA-40 re-analysis. Q J R Meteorol Soc 131:2961–3012. DOI 10.1256/qj.04.176

Vogelezang DHP, Holtslag AAM (1996) Evaluation and model impacts of alternative boundary-layer height formulations. Bound Layer Meteorol 81:245–269

Webb M, Senior C, Bony S, Morcrette J-J (2001) Combining ERBE and ISCCP data to assess clouds in the Hadley Centre ECMWF and LMD atmospheric climate models. Clim Dyn 17:905–922

Wentz FJ (1997) A well calibrated ocean algorithm for special sensor microwave/imager. J Geophys Res 102:8703–8718

Williams KD, Ringer MA, Senior CA (2003) Evaluating the cloud response to climate change and current climate variability. Clim Dyn 20:705–721

Wood R, Bretherton CS, Hartmann DL (2002) Diurnal cycle of liquid water path over the subtropical and tropical oceans. Geophys Res Lett 29(23):2093. DOI 10.1029/2002GL015371

Zhang GJ, McFarlane NA (1995) Sensitivity of climate simulations to the parameterization of cumulus convection in the Canadian Climate Center general circulation model. Atmos Ocean 33:407–446

Zhang MH, Lin W, Bretherton CS, Hack JJ, Rasch PJ (2003) A modified formulation of fractional stratiform condensation rate in the NCAR community atmospheric model CAM2. J Geophys Res 108(D1):4035. DOI 10.1029/2002JD002523

Zhang MH et al (2005) Comparing clouds and their seasonal variations in 10 atmospheric general circulation models with satellite measurements. J Geophys Res D15S02. DOI 10.1029/2004JD005021